

See discussions, stats, and author profiles for this publication at: <https://www.researchgate.net/publication/264251883>

Hierarchically Structured Zeolite Bodies: Assembling Micro-, Meso-, and Macroporosity Levels in Complex Materials with Enhanced Properties

ARTICLE *in* ADVANCED FUNCTIONAL MATERIALS · JUNE 2012

Impact Factor: 11.81 · DOI: 10.1002/adfm.201103120

CITATIONS

12

READS

32

9 AUTHORS, INCLUDING:



[Nina-Luisa Michels](#)

ETH Zurich

10 PUBLICATIONS 206 CITATIONS

SEE PROFILE



[Sharon Mitchell](#)

ETH Zurich

49 PUBLICATIONS 504 CITATIONS

SEE PROFILE



[Javier Pérez-Ramírez](#)

ETH Zurich

308 PUBLICATIONS 8,457 CITATIONS

SEE PROFILE

Hierarchically Structured Zeolite Bodies: Assembling Micro-, Meso-, and Macroporosity Levels in Complex Materials with Enhanced Properties

Nina-Luisa Michels, Sharon Mitchell, Maria Milina, Karsten Kunze, Frank Krumeich, Federica Marone, Mandy Erdmann, Nadia Marti, and Javier Pérez-Ramírez*

Engineering levels of porosity in hierarchical zeolites is a vibrant area of research with remarkable application potential. To gain practical relevance, the superior properties observed for the as-synthesized powders have to be preserved when they are shaped into suitable technical geometries. Herein, mechanically stable millimeter-sized bodies are prepared by granulation of mesoporous ZSM-5 zeolite powders using an attapulgite clay binder. Alkaline treatment of conventional zeolite granules is demonstrated to be unsuitable for this purpose. Multiple techniques are applied to characterize mesoporous zeolite granules with respect to their conventional zeolite counterparts, thus establishing the impact of binder inclusion and granulation on their respective properties. The intrinsic structure and acidity of the zeolite are retained post-structuring. Gas adsorption and mercury porosimetry confirm the presence of interconnected micro-, meso-, and macropores. A wide range of imaging techniques permits visualization of the particle properties, phase distribution, and consequent origins of the distinct levels of porosity within the zeolite granules. The superior adsorption properties of the hierarchical ZSM-5 zeolite granules are demonstrated using cyclohexane, toluene, and isopropyl alcohol as probe molecules.

1. Introduction

A major goal in materials science is to control the hierarchical organization of functional solids from the atomic to the macroscopic scale. Multilevel architectures offer unique

catalytic, electronic, optical, and magnetic properties.^[1] One prominent example is the assembly of hierarchical levels of porosity in zeolites. These crystalline microporous aluminosilicates are exemplary heterogeneous catalysts and adsorbents.^[2] Nevertheless, their performance can be remarkably enhanced by introduction of an auxiliary mesopore network, due to the improved access and transport of reactant and product molecules.^[3]

A wide variety of bottom-up and top-down approaches exist to prepare mesoporous zeolite powders on a laboratory scale.^[3–5] However, the transfer of most of these methods to the technical scale is challenging with respect to procedural complexity and economic feasibility. Exceptionally, desilication, that is, the controlled leaching of framework silicon by alkaline treatment, was recently demonstrated as a scalable and cost-effective post-synthetic route to prepare mesoporous ZSM-5 zeolite powders.^[6]

Fine powdered materials are unsuitable for many industrial processes, as they do not comply with process requirements, in terms of mechanical stability, pressure drop, mass transfer, recoverability, and economics.^[7,8] An integral part of catalyst or sorbent manufacture is their structuring into practical millimeter-sized geometries (granules, pellets, extrudates, etc.), which is achieved by addition of binders (e.g., clays, silicas, or aluminas) and other additives followed by shaping using different methods.^[8] This step is crucial for the successful scale up of any promising zeolite formulation and introduces substantial complexity.^[9] The structuring of powders into consolidated bodies is predominantly carried out by industry and is surrounded by trademark secrecy. Generally, there is a remarkable lack of fundamental understanding with respect to the preparation and characterization of shaped catalysts and sorbents.

In order to advance in the scale up and ultimate implementation of hierarchical zeolites, a robust preparation protocol must be identified and the impact of binder inclusion and shaping on the properties of the mesoporous zeolites investigated. The organization of porosity levels starting from the intracrystalline micro- and mesopores (nm) and extending through the interparticle meso-macro network (μm) to the exterior should therein be mastered.

In this work, two independent strategies for the preparation of hierarchical zeolite granules are compared: i) the desilication of conventional zeolite granules and ii) the structuring of

N.-L. Michels, Dr. S. Mitchell, M. Milina,
Prof. J. Pérez-Ramírez
Institute for Chemical and Bioengineering
Department of Chemistry and Applied Biosciences
ETH Zürich, Wolfgang-Pauli-Strasse 10,
8093 Zürich, Switzerland
E-mail: jpr@chem.ethz.ch

Dr. K. Kunze
Electron Microscopy Center ETH Zürich
Wolfgang-Pauli-Strasse 16, 8093 Zürich, Switzerland

Dr. F. Krumeich
Laboratory of Inorganic Chemistry
Department of Chemistry and Applied Biosciences
ETH Zürich, Wolfgang-Pauli-Strasse 10, 8093 Zürich, Switzerland

Dr. F. Marone
Swiss Light Source, Paul Scherrer Institute
5232 Villigen, Switzerland

Dr. M. Erdmann, Dr. N. Marti
Zeochem AG, Seestrasse 108, 8707 Uetikon, Switzerland



DOI: 10.1002/adfm.201103120

mesoporous ZSM-5 powders. The physicochemical properties of conventional and alkaline-treated zeolite powders and granules are characterized by multiple techniques to assess their structure, porosity, acidity, and mechanical stability. State-of-the-art imaging techniques are applied to visualize the spatial distribution of zeolite and binder phases and the associated porosity levels. The shaped mesoporous zeolites are applied in adsorption studies with cyclohexane, toluene, and isopropyl alcohol. Thereby, the preservation of the outstanding properties and functionalities of mesoporous zeolites during the progression from powders to hierarchically structured bodies is demonstrated.

2. Results and Discussion

2.1. Preparation of Hierarchical ZSM-5 Granules

Conventional zeolite granules (CGc) of 2–3 mm diameter were obtained following a standard industrial protocol (Figure 1)

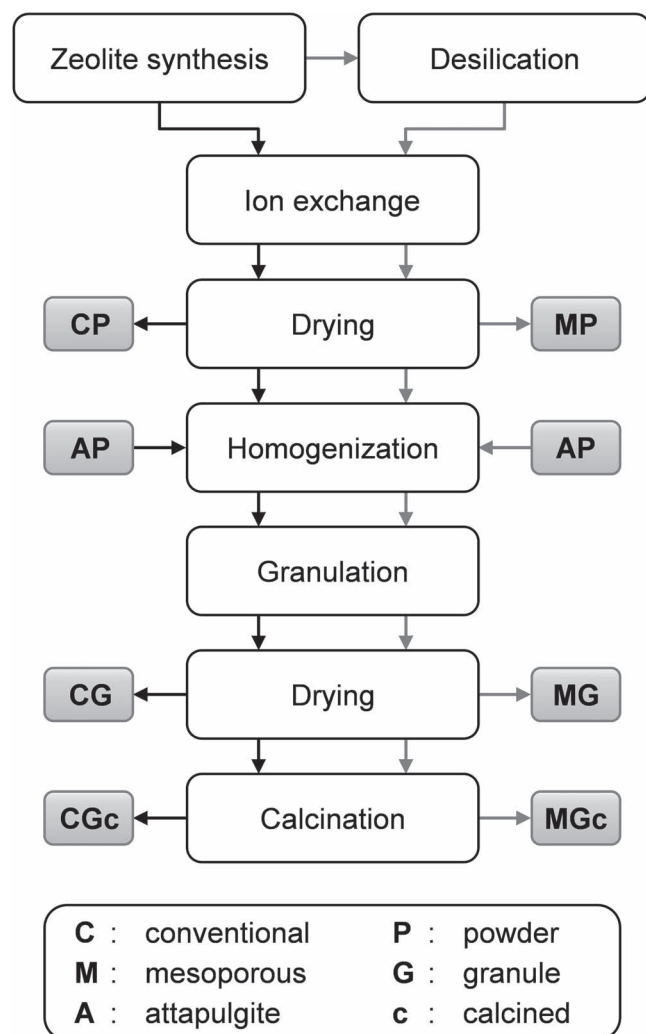


Figure 1. Steps in the preparation of conventional and hierarchical zeolite granules and key samples derived. The significance of the codes is indicated in the bottom panel.

using high-purity attapulgite ($\text{Mg,Al}_2\text{Si}_4\text{O}_{10}(\text{OH}) \cdot 4\text{H}_2\text{O}$) as the binder (zeolite:binder dry mass ratio 80:20). Two strategies were considered for the preparation of hierarchical ZSM-5 granules (Figure 2): the alkaline treatment of conventional zeolites granules (route 1) and the granulation of desilicated zeolite powders with attapulgite (route 2). Route 1 led to disintegration of the granules, as seen by the generation of fine powdered material, even under mild stirring conditions. No significant dissolution was observed upon alkaline treatment of the pure attapulgite binder (yield ca. 86 wt%), indicating that the loss of structural integrity was most likely associated with the weakening of interparticle interactions due to hydrolysis in the alkaline solution rather than leaching of the binder. Mesoporosity introduction was also less effective in the granule form with respect to desilication of the conventional zeolite powder (CP), leading to mesoporous surface areas (S_{meso}) of 128 and 197 $\text{m}^2 \text{g}^{-1}$, respectively. Therefore, this route was rejected after preliminary trials.

Appropriate quantities of mesoporous zeolite powder for granulation (ca. 2 kg) were obtained by pilot-scale alkaline treatment of the purely microporous CP ($\text{Si}/\text{Al} = 39$).^[6] No significant variation in the average particle size distribution was observed following post-synthetic modification (Supporting Information, Figure S11). The mesoporous zeolite powder (MP) was structured according to the same protocol applied for the granulation of the conventional zeolite (Figure 1). The most noticeable difference encountered was the larger quantity of water (ca. 30%) needed to initiate granule formation. This was attributed to the increased pore volume of MP due to the presence of the intracrystalline mesopores (Table 1).

The binder plays an important role in determining the properties of the resulting zeolite granules. During granulation the “nests” of aggregated binder particles, observed in the as-received powder (Supporting Information, Figure S12), were dispersed and covered the surface of the zeolite particles. The distinctive needle-like particle morphology of the binder facilitated phase identification during microscopic studies. Calcination to increase the mechanical strength of the granules led to decomposition of the attapulgite, but did not vary the inherent porous properties (Supporting Information, Figure S13a,b), resulting in an amorphous mixed oxide phase (vide infra). A detailed characterization of the as-received and calcined attapulgite powder is provided in the Supporting Information.

2.2. Porous Properties

The porous properties of the powders and granules were assessed by combined gas adsorption (Ar and N_2) and mercury porosimetry (Table 1). The zeolite powders exhibited micropore volumes ($V_{\text{micro}} = 0.16$ and $0.12 \text{ cm}^3 \text{g}^{-1}$) and mesoporous surface areas ($S_{\text{meso}} = 77$ and $207 \text{ m}^2 \text{g}^{-1}$) typical of those expected for conventional and mesoporous ZSM-5, respectively.^[5] Comparison of the Ar and N_2 isotherms (Figure 3a,b) shows that MPc exhibits significantly increased Ar and N_2 uptakes, which is especially noticeable at high relative pressures ($p/p_0 \geq 0.6$).

Upon granulation, a good agreement is observed between the porous characteristics derived from the measured data and those calculated based on the proportional contributions of the calcined zeolite and binder phases. The slight reduction in the

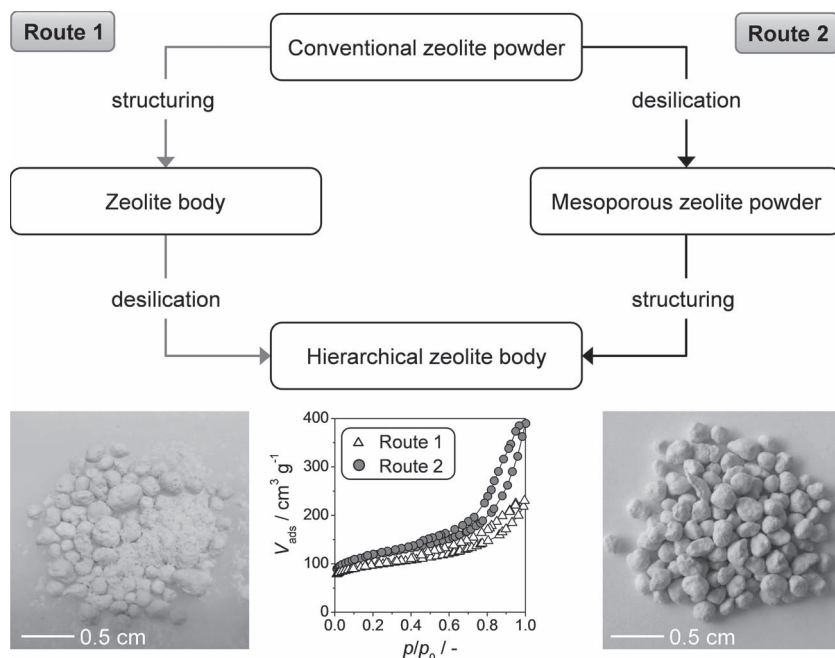


Figure 2. Strategies for the preparation of hierarchical zeolite granules. Photographs of hierarchical granules obtained by route 1 (left) or route 2 (right) and corresponding N₂ isotherms (center).

micropore volume of both CGc and MGc with respect to CPC and MPC result from the presence of the binder, which is not microporous. No pore blockage due to interaction of the zeolite with the binder was evidenced.

The substantially higher mesoporous surface area of MGc than CGc ($S_{\text{meso}} = 91$ and $197 \text{ m}^2 \text{ g}^{-1}$, respectively) confirmed that the intracrystalline mesoporosity of the zeolite is maintained post-structuring. Incorporation of the attapulgite, which has a slightly lower mesoporosity ($S_{\text{meso}} = 125 \text{ m}^2 \text{ g}^{-1}$), led to a small reduction in mesoporosity of MGc with respect to MPC. In the case of CGc, binder inclusion had a favorable impact on the mesoporosity due to the lower mesoporous surface area of the conventional zeolite powder ($S_{\text{meso}} = 77 \text{ m}^2 \text{ g}^{-1}$). A clear fingerprint of the binder contribution is seen at high relative pressures in the corresponding N₂ isotherm (Figure 3b).

Mercury porosimetry provided complementary assessment of the meso- and macroporosity (Figure 4).^[10] All zeolites exhibited

a single intrusion step in the macropore filling region. An additional intrusion step is observed in the desilicated ZSM-5 powders and granules in the high-pressure region ($>30 \text{ MPa}$), consistent with the presence of intracrystalline mesopores. The estimated mesopore volume was $0.35 \text{ cm}^3 \text{ g}^{-1}$ (Table 1). Upon granulation, the first intrusion step shifted to higher pressures (Figure 4a,b), a direct consequence of the definition of a new interparticle macropore network. Quantification of the intrusion curves of CGc and MGc led to macropore volumes of 0.27 and $0.32 \text{ cm}^3 \text{ g}^{-1}$, respectively (Table 1), inferring similar granulation behavior. The complete reversibility of mercury intrusion during two consecutive cycles on MGc confirmed the structural stability of the intra-granule pore system (Figure 4c).

Analysis of the pore size distributions derived from the Ar and N₂ isotherms and the mercury intrusion curves (Figure 5) demonstrated the complementarity of the techniques. Whereas a bimodal pore distribution is observed in the case of CGc, composed of micropores intrinsic to the zeolite phase and interparticle macropores between the zeolite and binder particles, the trimodal porosity of MGc due to the presence of intracrystalline mesopores is clearly revealed. The hierarchical pore architecture consists of micro-, meso-, and macropores centered around 0.5 , 10 , and 150 nm , respectively (Figure 5b). The average intracrystalline mesopore diameter of MGc was equivalent to MPC. The slight deviation in the pore size distributions estimated by the Barrett-Joyner-Halenda (BJH) model and non-local density functional theory (NLDFT) arises due to the differing assumptions of the respective models.^[11] The peak at around 0.8 nm in the NLDFT pore size distribution is an artifact associated with the phase transition of Ar in ZSM-5 zeolites and does not result from the presence of pores of this size.^[12]

2.3. Mechanical Properties

Structured zeolites must be stable under the conditions of industrial operation. The mechanical stability of mesoporous and conventional zeolite granules was characterized by evaluation of their crush strength and attrition resistance. MGc exhibited a crush strength of 12 N , which is equivalent to that of CGc (Table 1). Such values are typical for granules produced on pilot-scale. Testing of the attrition index indicated a very high resistance, with MGc producing only 0.40% in comparison with 0.64% fines lost by the conventional analogues. These observations are a good indication that the introduction of intracrystalline mesoporosity will most likely not be detrimental to the mechanical properties of structured zeolites when manufactured at an industrial scale.

Table 1. Characterization data of the zeolite granules and their powder constituents.

Sample code	Si/Al ^{a)} [-]	$V_{\text{pore}}^{\text{b)}$ [$\text{cm}^3 \text{ g}^{-1}$]	$V_{\text{micro}}^{\text{c)}$ [$\text{cm}^3 \text{ g}^{-1}$]	$S_{\text{meso}}^{\text{d)}$ [$\text{m}^2 \text{ g}^{-1}$]	$S_{\text{BET}}^{\text{d)}$ [$\text{m}^2 \text{ g}^{-1}$]	$V_{\text{meso}}^{\text{e)}$ [$\text{cm}^3 \text{ g}^{-1}$]	$V_{\text{macro}}^{\text{f)}$ [$\text{cm}^3 \text{ g}^{-1}$]	Crush strength [N]
APc	—	0.43	0.00	125	125	0.29	—	—
CPc	39	0.27	0.16	77	449	0.04	—	—
CGc	32	0.32 (0.30) ^{g)}	0.13 (0.13)	91 (87)	394 (384)	0.13	0.27	12
MPC	28	0.61	0.12	207	496	0.35	—	—
MGc	23	0.56 (0.57)	0.09 (0.10)	197 (191)	428 (422)	0.37	0.32	12

^{a)}Molar ratio in the solid, determined by AAS; ^{b)}Volume of N₂ adsorbed at $p/p_0 = 0.99$; ^{c)}t-plot method; ^{d)}BET (Brunauer-Emmett-Teller) method; ^{e)}Volume of Hg intruded into pores of $3.7\text{--}50 \text{ nm}$ diameter; ^{f)}Volume of Hg intruded into pores of $>50 \text{ nm}$ diameter; ^{g)}In parenthesis, calculated values based on the proportional contribution of component species (20 wt% attapulgite and 80 wt% zeolite).

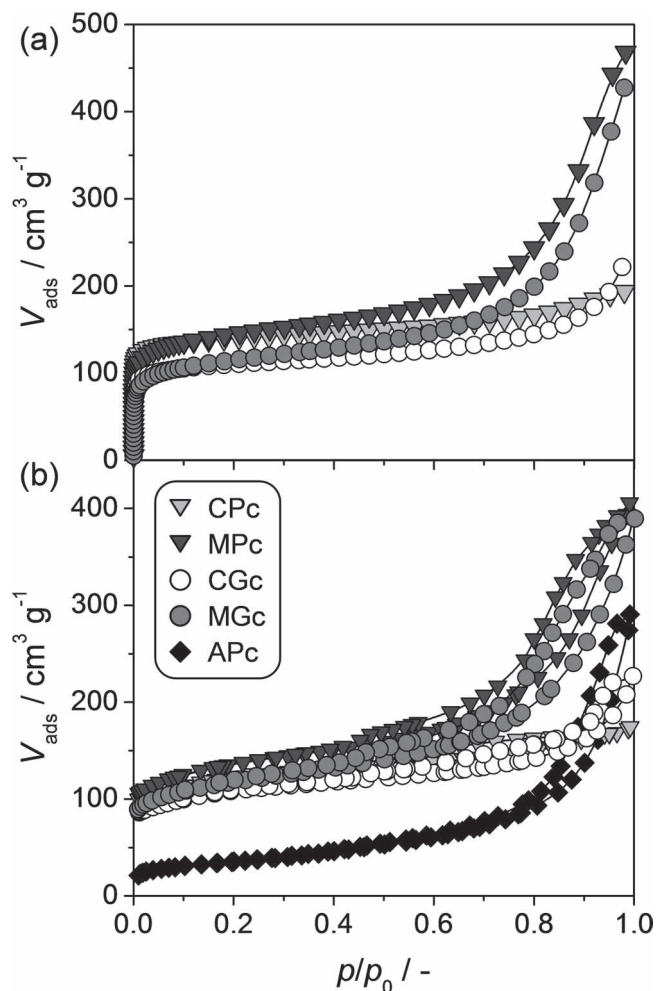


Figure 3. Ar isotherms at 87 K (a) and N_2 isotherms at 77 K (b) of the conventional and mesoporous ZSM-5 granules and their powder constituents.

2.4. Visualization

The hierarchical zeolites granules were examined using a battery of imaging techniques to characterize the particle properties, to study the particle agglomeration and phase distribution resulting from granulation, and to confirm the origin of the distinct levels of porosity identified in Section 2.2.

Granules of approximately spherical shape and uniform surface roughness were observed by optical microscopy as shown in the montage image of a single granule of MGc (Figure 6a). Synchrotron-based X-ray tomographic microscopy (SRXTM) permitted rapid 3D imaging of the interior structure of the whole granules by non-destructive means, with a resolution down to the sub-micrometer scale.^[13] 2D virtual slices computed from the 3D tomographic dataset obtained appeared uniform throughout the conventional and mesoporous zeolite granules studied (Figure 6b,c, respectively). This demonstrates the homogeneous phase distribution of the binder and zeolite particles and further supported the similar agglomeration behavior of CPc and MPc. In the

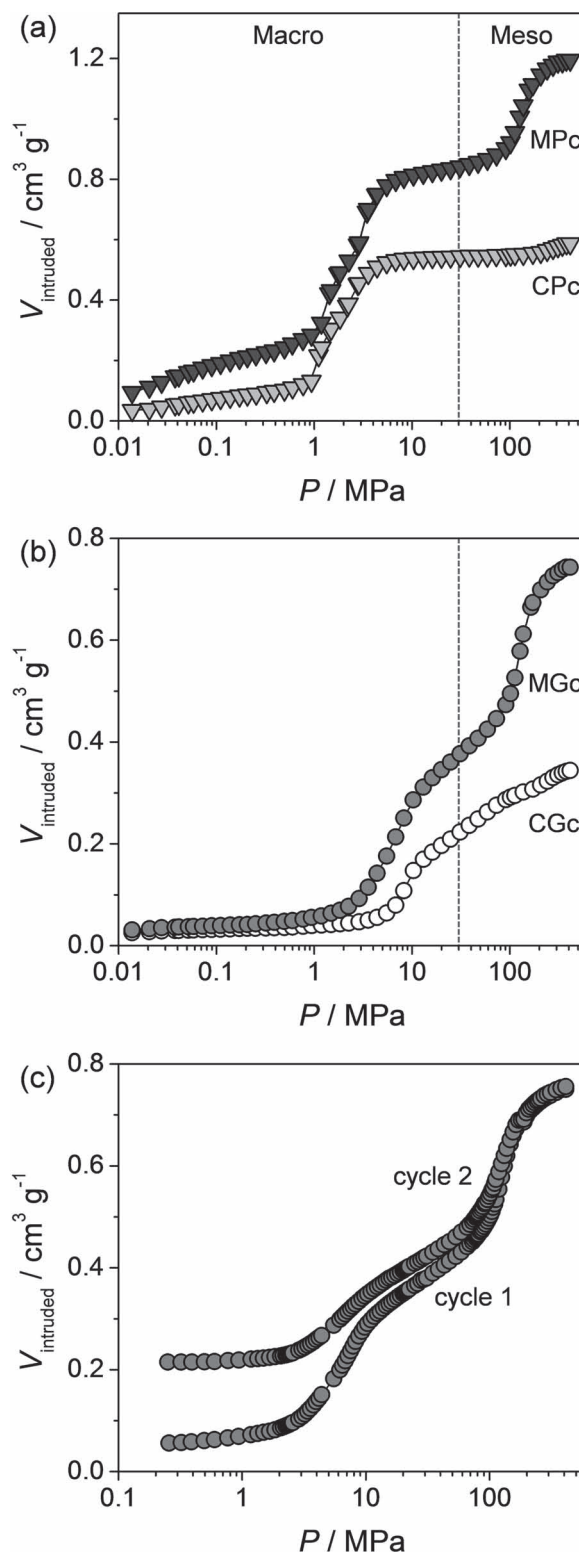


Figure 4. Hg intrusion curves of the conventional and mesoporous ZSM-5 powders (a) and granules (b). Reproducibility of consecutive Hg intrusion cycles on MGc (c).

case of CGc, rounder particle-like structures (ca. 2–4 μm) are clearly identifiable, appearing with lighter contrast due to

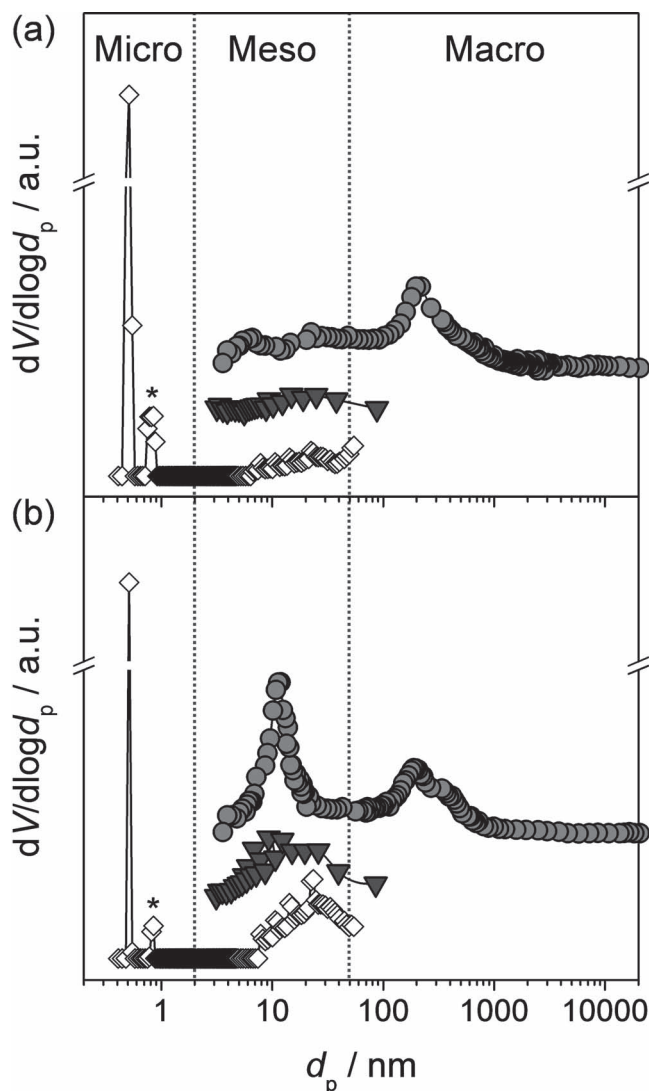


Figure 5. Comparative pore size distributions of CGc (a) and MGc (b) derived from the Ar (NLDFT analysis, white diamonds) and N₂ (BJH model, grey triangles) adsorption, and Hg intrusion (Washburn equation, grey circles), respectively. The plots are offset for clarity. The peak with the asterisk is an artifact associated with a phase transition of Ar.

their denser and therefore more adsorbing nature. Between the particles regions of lighter grey contrast and black areas are observed. The black features are connected throughout the entire granule when reconstructed into a 3D image, and represent the macropore network, i.e., the intragranular space between the zeolite particles and the binder. Differences are observed on comparison of the tomograms of MGc and CGc. Individual particles are not as readily distinguishable in the SRXTM image of MGc as of CGc, and circular features are visible.

Further differences were observed in confocal fluorescence microscopy (CFM) images of the granules stained with a combination of dyes, thiophene (green fluorescence), and Nile blue (red fluorescence).^[14] Whereas thiophene is converted to fluorescent products over Brønsted acid sites only (after reaction

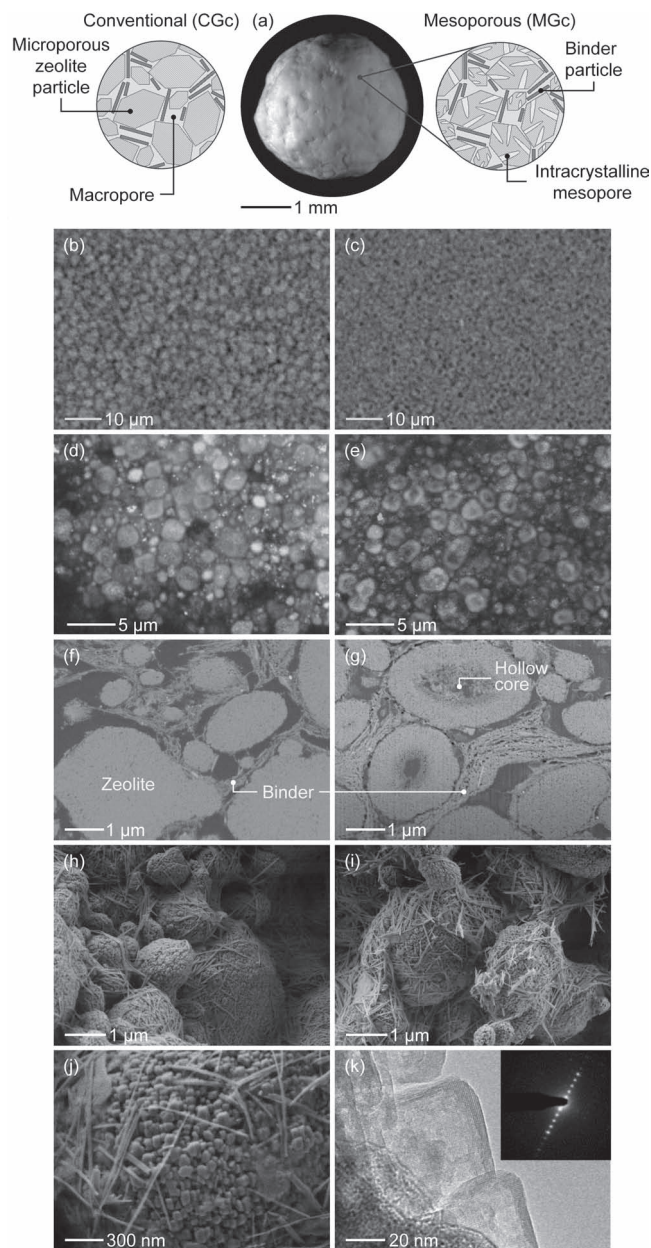


Figure 6. Montage optical microscopy image of a mesoporous zeolite granule (a), 2D virtual slices computed from 3D SRXTM of CGc (b), and MGc (c). Confocal fluorescence microscopy images of stained conventional (d) and mesoporous (e) ZSM-5 granules. SEM images of FIB-prepared cross-sections of CGc (f) and MGc (g). SEM images of CGc (h,i) and MGc (i) and HRTEM image of mesoporous ZSM-5 (k) with SAED pattern (inset).

at 337 K),^[15] the unreactive Nile blue is too large to enter the zeolitic micropores and stains the binder as well as the exterior surface of the zeolite particles. Comparison of the fluorescence images of CGc with respect to MGc (Figure 6d,e) shows that while the conventional zeolite particles exhibit uniform fluorescence, the larger mesoporous zeolite particles appear to have donut-like shapes, in accordance with the circular features observed by SRXTM.

The internal organization of the granules was further characterized by applying dual focused ion beam-scanning electron microscopy (FIB-SEM) to image successive cross-sectional areas of resin-embedded granules. The binding matrix can be clearly identified in the microscopy images obtained (Figure 6f,g), wrapped around the zeolite particles in both CGc and MGc. This explained the regions of lighter grey contrast observed by SRXTM. The intimate contact between the highly dispersed needles of the attapulgite-derived binder and the zeolite particles was clearly revealed in the high-resolution SEM images of CGc and MGc (Figure 6h,i). At higher magnifications individual zeolite crystals of ca. 50–70 nm width were evidenced (Figure 6j). The crystallinity of the zeolite is confirmed by observation of lattice fringes in high-resolution transmission electron microscopy (HRTEM) and of a sharp diffraction pattern measured by selected area electron diffraction (SAED; Figure 6k).

Larger mesoporous zeolite particles (Figure 6g) were found to exhibit hollow centers, which were not present in the conventional zeolite (Figure 6f) and are evidence for the origin of the unexpected differences observed between MGc and CGc by SRXTM and CFM. The additional presence of macroporous cavities could explain the slightly increased macropore volume ($0.05 \text{ cm}^3 \text{ g}^{-1}$) of the mesoporous zeolite granule (Table 1). Smaller zeolite particles (ca. $0.5 \mu\text{m}$) do not display this feature. Since CGc and MGc were structured equivalently, the origin of

the “hollow” particles can be related to the process of desilication by alkaline treatment.

Aluminum zoning is commonly observed in ZSM-5 zeolites and is known to give rise to non-uniform mesoporosity development upon alkaline treatment due to the preferential dissolution of siliceous-rich areas.^[16,17] For large single crystals, surface enrichment of aluminum led to the formation of zeolites with hollow cores.^[17] In the present study, a narrow crystalline rim ($\approx 10 \text{ nm}$ wide) is observed in individual MPc particles by HRTEM (Figure 6k), which is related to the presence of an Al-rich zone in CPC. At a particle level, the differences observed in dissolution behavior indicate that the presence of concentration gradients not only exists at the crystal level, but also on a macroscopic scale, with crystallites located in the center of the aggregate having a higher Si/Al molar ratio than those located around the periphery. Large compositional variations were not obvious in the combined elemental maps of Si and Al obtained by energy-dispersive X-ray (EDX) spectroscopic analysis of FIB-prepared cross-sections of CGc and MGc (Figure 7a,b, respectively). However, in contrast to previous work,^[17] the sizes of both the individual and the aggregated zeolite crystals studied here are considerably smaller. As the determination of Al gradients is limited by the spatial resolution of EDX, the detection at the nanometer scale is challenging and therefore their presence cannot be excluded.^[18]

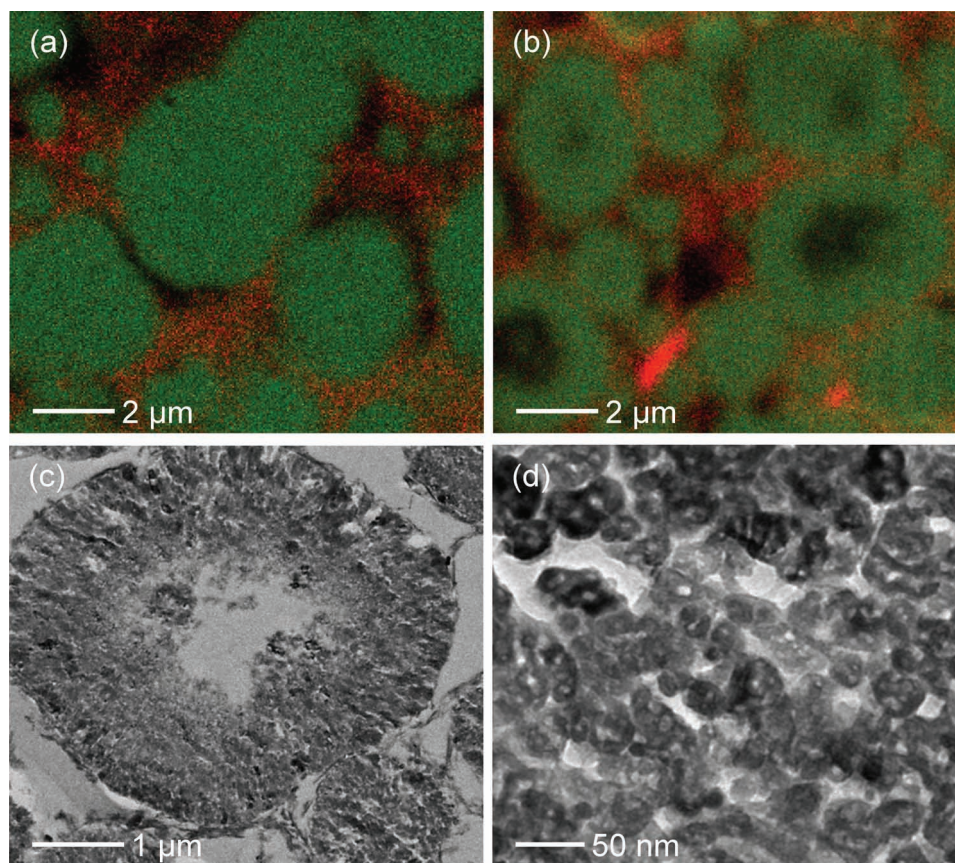


Figure 7. Combined elemental maps of Si (green) and Al (red) measured by EDX spectroscopic analysis of FIB-prepared cross-sections of CGc (a) and MGc (b). TEM images of ultrathin cross-section of resin-embedded MGc (c,d).

Studies of ultrathin cross-sections of resin-embedded MGc by TEM further evidenced the presence of hollow centers in large mesoporous zeolite aggregates. Mesopores were seen to extend from the external surface of the particle towards the interior cavity (Figure 7c). At higher magnifications, individual crystals of approximately 50 nm in diameter with highly beam-transparent centers were observed (Figure 7d). This could be attributed to preferential dissolution of the crystal interior and an Al-rich edge, in agreement with the findings of HRTEM (Figure 6k).

2.5. Structure and Acidity

Structuring has no effect on the zeolite crystallinity, as evidenced by X-ray diffraction (XRD) (Figure 8a). The decreased reflection intensity observed for PGc and MGc with respect to CPc and MPc results from the inclusion of the attapulgite and is proportional to the binder content in the granules. Following calcination the binder itself is amorphous. The small reflections observed in the diffraction patterns correspond to a trace amount of a quartz impurity. The slightly lower crystallinity of MPc with respect to CPc is a common observation for alkaline-treated zeolites.^[5]

Possible impacts of structuring on the acidic properties were investigated by using ^{27}Al and ^{29}Si magic angle spinning (MAS)

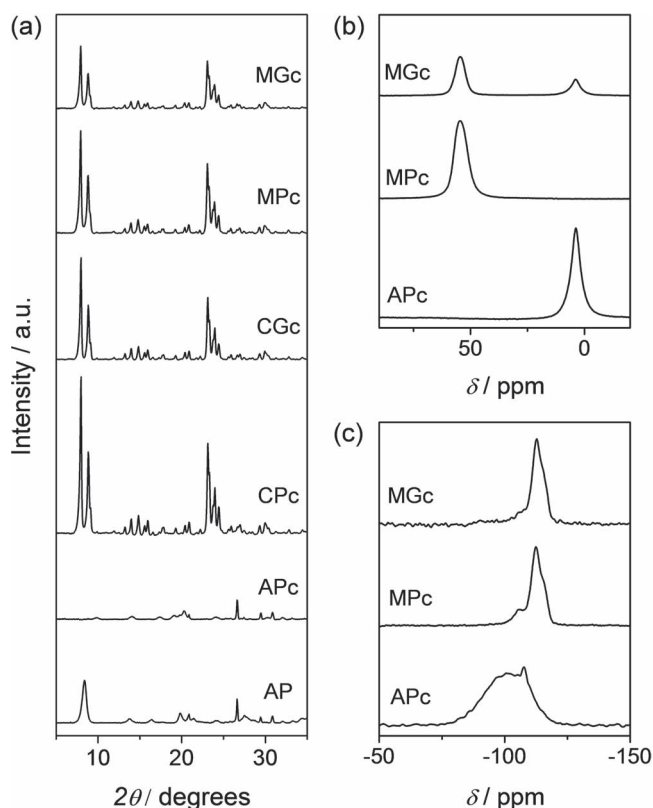


Figure 8. XRD patterns of conventional and mesoporous ZSM-5 powders and granules (a). The XRD pattern of the attapulgite binder before and after calcination is shown for comparison. ^{27}Al (b) and ^{29}Si (c) MAS NMR spectra of MPc, MGc, and APc.

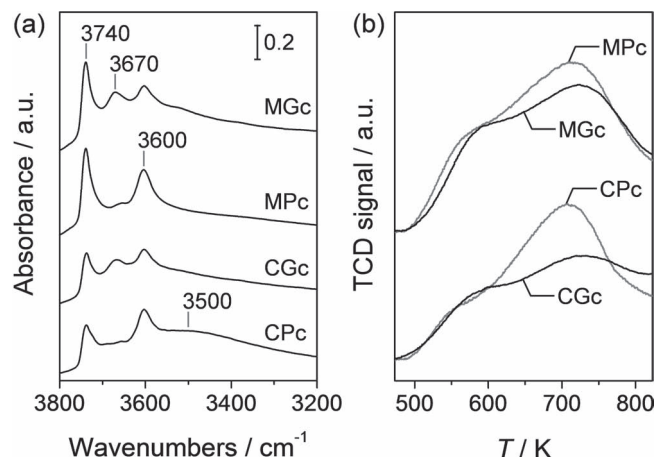


Figure 9. Infrared spectra in the hydroxyl stretching region (a) and NH_3 -TPD profiles (b) of conventional and mesoporous ZSM-5 powders and granules.

NMR, Fourier transform infrared (FTIR) spectroscopy in the OH stretching region, and temperature-programmed desorption of ammonia (NH_3 -TPD). The ^{27}Al MAS NMR spectrum of MPc exhibited a single peak at 55 ppm corresponding to aluminum in tetrahedral coordination in the framework. No evidence of extra-framework aluminum in octahedral coordination (0 ppm) was detected. The appearance of a peak at 0 ppm in the ^{27}Al MAS NMR spectrum MGc (Figure 8b) occurred due to the presence of octahedrally coordinated aluminum in the binder. No significant variation was observed in the ^{29}Si MAS NMR spectra of MGc (Figure 8c), which reflects a combination of the two phases.

The FTIR spectra (Figure 9a) of the pure zeolite powders are exemplary for those expected of purely microporous and alkaline-treated ZSM-5.^[10] A decreased intensity of the band at 3600 cm^{-1} , characteristic of Brønsted acidity, is observed upon granulation of both the conventional and mesoporous zeolite, as the attapulgite-derived binder showed no absorbance in this range (Supporting Information Figure SI3c). This effect was proportional to the content of the binder, which “dilutes” the strong zeolitic acidity. Moreover, no evidence of dealumination of the zeolite framework, as a consequence of steaming during hardening by calcination, was detected.

A similar diluting effect was observed by NH_3 -TPD (Figure 9b). The high-temperature desorption peak (ca. 720 K) in the profile of both the mesoporous and conventional granules, primarily associated with strong Brønsted acid sites, was reduced with respect to those of the pure zeolite powders. No significant variation could be observed for the low-temperature desorption peak (shoulder at ca. 570 K), often attributed to the presence of weaker acid sites of Lewis character.

2.6. Adsorption Properties

Gravimetric adsorption studies of cyclohexane, toluene, and isopropyl alcohol were undertaken to assess molecular adsorption in shaped mesoporous zeolites. These molecules are representative of cyclic alkanes, aromatics, and alcohols and possess

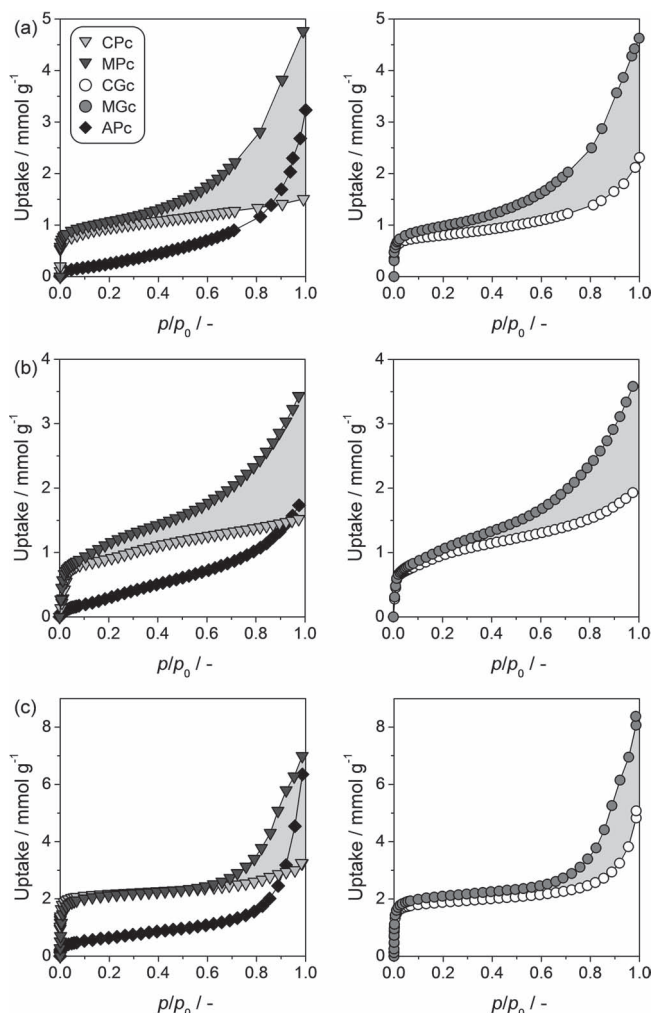


Figure 10. Adsorption isotherms of cyclohexane (a), toluene (b), and isopropyl alcohol (c) on the powder components (left column) and granules (right column) of conventional and mesoporous zeolites.

kinetic diameters of 0.60, 0.61, and 0.47 nm, respectively. All three adsorbates are able to penetrate the ZSM-5 micropores. The equilibrium adsorption isotherms obtained for mesoporous and conventional zeolite granules and for their powder components are shown in **Figure 10**.

Conventional ZSM-5 powders exhibited pseudo-Langmuir type I behavior, independent of the adsorptive studied. The largest uptake was observed at low relative pressures, associated with micropore filling. Mesoporous zeolite powders feature type I/IV characteristics. In addition to showing similar uptakes with respect to their conventional counterparts at low relative pressures, significant uptakes were also observed at higher relative pressures, arising from the filling of the mesopores. The adsorption capacity was more than doubled following the introduction of mesoporosity by desilication (**Figure 11**). Here, the main differences between the adsorptives were the total uptakes and the shape of the isotherms, which showed varying slope. The former is strongly related to the molecular size, with the smaller isopropyl alcohol molecule exhibiting the highest uptake. The difference in behavior on mesopore filling

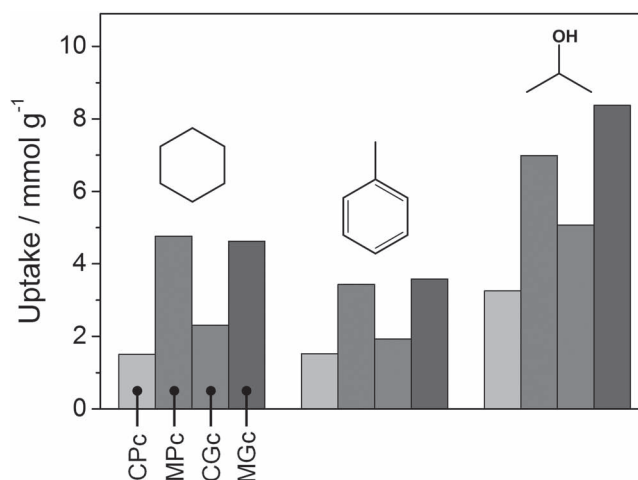


Figure 11. Adsorption capacities of cyclohexane, toluene, and isopropyl alcohol investigated on conventional and mesoporous ZSM-5 powders and granules.

results from variations in adsorbate–adsorbent and adsorbate–adsorbate interactions. Overall, the adsorption affinity followed the trend: toluene > cyclohexane > isopropyl alcohol.

Adsorption isotherms of the attapulgite-derived binder displayed a gradual increase, with larger uptakes at relative pressures, corresponding to type II behavior. The adsorption affinity of the three probe molecules showed similar trends to those observed for mesoporous zeolite powders.

The small reduction in the low pressure uptake of conventional and mesoporous zeolite granules (**Figure 10**) resulted from incorporation of the binder. However, this is proportional to the binder content, implying that the micropores remained accessible to larger molecular species. The most noticeable change in adsorption behavior upon structuring was observed for CGc, which exhibited an increased uptake at high relative pressures. This resulted in a gain in adsorption capacity of approximately 30%. Similar findings have been reported in previous studies.^[19–21] This highlights that the binder identity and its related porous properties are important in determining the overall performance. For the mesoporous zeolites, no such beneficial increase was seen due to the lower relative porosity of the binder. However, the hierarchically structured granules preserve their superior adsorption capacities with respect to the conventional zeolites. MGc exhibited increased adsorption capacities with respect to CGc of 50% for cyclohexane, 46% for toluene, and 40% for isopropyl alcohol (determined at $p/p_0 = 0.99$). Structuring mesoporous zeolite powders into granules and the consequent (zeolite–binder) interparticle interactions do not interfere with the adsorption of the selected probe molecules.

3. Conclusions

Mesoporous zeolite granules possessing interconnected micro-, meso-, and macropores were successfully prepared by structuring desilicated ZSM-5 powders with an attapulgite binder. Alkaline treatment of pre-formed conventional zeolite granules proved an impractical preparation strategy. Thorough characterization

confirmed the mechanical stability, the preserved acidity, and the truly hierarchical structure of the resulting materials. Neither the intracrystalline mesoporosity introduced by post-synthetic modification nor the intrinsic zeolite microporosity, were affected by binder inclusion or by the granulation process. Adsorption studies of three volatile organic compounds confirmed the enhanced adsorption capacities of the hierarchically structured ZSM-5 granules with respect to their conventional counterparts.

4. Experimental Section

Zeolite Synthesis and Desilication: ZSM-5 zeolite (Si/Al = 39) was hydrothermally synthesized in a pilot-scale reactor at Zeochem's production site (Uetikon, Switzerland), using tetrapropylammonium cation as the templating agent. The conditions are detailed elsewhere.^[6] Template removal was achieved by calcination in flowing dry air at 753 K for 3 h in a Nabertherm furnace. Desilication of the template-free Na-ZSM-5 was carried out in aqueous NaOH (0.2 M, 30 cm³ per gram of zeolite) in a batch reactor (50 L, Juchheim). The solution was heated to 338 K at a rate of 1 K min⁻¹, treated isothermally for 30 min, and then cooled at 1 K min⁻¹ under mechanical stirring.^[6] The alkaline-treated (mesoporous) zeolite powders were filtered, washed, converted into the ammonium form by a single ion exchange with aqueous NH₄NO₃ (0.1 M, 100 cm³ per gram of zeolite) for 6 h, and calcined under dry air circulation at 823 K for 5 h at 2 K min⁻¹.

Preparation of Zeolite Granules: The conventional and mesoporous zeolite powders in ammonium form were structured into mm-sized granules by using an Eirich pan granulator and a high-purity attapulgite clay (Mg,Al)₂Si₄O₁₀(OH)·4H₂O (supplied by Zeochem) as a binder (zeolite:attapulgite dry mass ratio of 80:20). The actual weight used was determined by the relative moisture of the solid at the time of mixing, which in turn was derived from the loss on ignition. In total, 2 kg of dry powder, composed of the mesoporous zeolite and attapulgite, was intensively mixed to achieve phase homogenization. Next, wet granulation was undertaken by stepwise addition of small quantities of Milli-Q water (1.5 L in total) to the physical mixture of attapulgite and mesoporous zeolite, followed by mixing using the integrated three component system of the Eirich granulator. This procedure was repeated until appropriately structured granules of ca. 1–5 mm in diameter were formed. The conventional zeolite powder serving as reference material was structured in a similar way, but with addition of 1 L of water in total. Finally, the granules were sieved (Retsch) to obtain the desired range of 2–3 mm in diameter and dried at 393 K for 12 h in a Nabertherm furnace under flowing dry air. Calcination was conducted in the same furnace using air convection at 823 K for 5 h at 5 K min⁻¹.

Desilication of Zeolite Granules: The desilication of conventional zeolite granules was undertaken at a laboratory scale under standard alkaline treatment conditions. Zeolite granules in the protonic form were treated in aqueous NaOH solution (0.2 M, 30 cm³ per gram of zeolite) at 373 K for 30 min under orbital shaking. The alkaline-treated granules were collected by filtration, washed with distilled water, and dried at 338 K for 12 h.

Porosity: Argon isotherms were recorded in a Micromeritics ASAP 2020 at 87 K. Prior to measurement, the samples were outgassed at 573 K for 8 h. The pore size distribution was obtained by non-local density functional theory (NLDFT) assessment of the adsorption isotherm.

Nitrogen sorption was performed in a Quantachrome Quadrasorb-SI gas adsorption analyzer at 77 K after evacuation of the samples at 573 K for 8 h. The mesopore size distribution was obtained by application of the Barrett-Joyner-Halenda (BJH) model to the adsorption branch of the isotherm.

Mercury intrusion porosimetry was performed with a Micromeritics Autopore IV 9510 operated in the pressure range from vacuum to 418 MPa. Samples were degassed in situ prior to measurement. A contact angle of 140° for mercury and a pressure equilibration time of 10 s were used. The pore size distribution was determined by application of the Washburn equation.

Mechanical Stability: The mechanical stability of the granulated samples was assessed by standard industrial tests. The average crush strength, derived from measurement of 20 individual granules, was determined using a tablet hardness tester (Dr. Schleuniger Pharamatron AG). The resistance to attrition was characterized by the weight loss upon vibrating the zeolite granules (100 g) in a Retsch sieving machine (500 µm mesh size, 20 cm i.d.) for 15 min in the presence of steel balls.

Microscopy and Tomography: Optical microscopy was conducted with a Leica M165 C stereoscope using incident light and a Plan Apochromat objective with 1× magnification.

Confocal fluorescence experiments were undertaken using a Zeiss LSM-510 META laser scanning microscope with a Plan Apochromat 100×/1.4 oil objective lens. Detection ranges of 500–550 nm and 660–737 nm were used upon excitation with lasers of $\lambda_{\text{ex}} = 488$ nm and $\lambda_{\text{ex}} = 633$ nm, respectively. Sample preparation included heating the granules to 373 K, addition of thiophene (Merck Chemicals), and reaction for a further 10 s. Subsequently, Nile blue (85% dye content, Sigma Aldrich), dissolved in ethanol, was added to the granules at ambient temperature.

SRXTM was performed at the TOMCAT beamline^[13] (2.9 T super bend photon source, critical energy 11.1 keV) at the Swiss Light Source (SLS). After penetration of the sample, X-rays were converted into visible light by a 20 µm thick Ce-doped LAG scintillator screen. Projection images were further magnified by microscope optics and digitized by a high-resolution charge coupled device (CCD) camera (PCO2000, PCO GmbH, Germany). The optical magnification was set to 20×, resulting in isotropic voxels of 370 nm in the reconstructed image (16-bit). For each volumetric data set, 3000 projections were recorded in equiangular steps over 180° at a photon energy of 15 keV using an exposure time of 200 ms. The images were post-processed online into flat- and darkfield-corrected sinograms^[22] and reconstructed using a highly optimized routine based on the Fourier method.^[23] 2D virtual slices derived from the tomographic datasets were analyzed and manipulated computationally using the Amira software.

Dual-beam FIB-SEM was performed using a Zeiss NVision 40 instrument equipped with an energy selective backscattered electron detector operated at 2 kV. Sample preparation comprised embedding the zeolite granules in a resin (HM-20 low viscosity-epoxy, Gurit) and edge trimming by a microtome (Ultracut). Cross-sections of the embedded granules were cut by FIB and immediately imaged by SEM.

SEM images of resin-embedded granules (G1 epoxy, Gatan) were acquired using a Zeiss Gemini 1530 FEG microscope operated at 1 kV.

HRTEM and SAED measurements were undertaken with a FEI Tecnai F30 microscope operated at 300 kV.

Energy-dispersive X-ray spectroscopic mapping (EDX) was conducted using the FEI Quanta 200FEG equipped with an EDX detector of SDD type (Ametek EDAX Apollo X). Sample preparation included microtome trimming surfaces of resin-embedded zeolite granules, followed by FIB-polishing at shallow incidence angle, and finally coating the sample by carbon evaporation (ca. 10 nm thick). The SEM was operated at 5 kV, spot 5 (nominal beam current of 6 nA with an 8 nm diameter); and the EDX using a count rate of 4000 cps, a map matrix 512 × 400, a pixel size of 32 nm, drift correction, a mapping time of ca. 10 h, and hyperspectral data acquisition. Analyzed data was reported in net intensities and ZAF-based concentrations (in weight percent) using a 3 × 3 pixel averaging mask.

Ultrathin cross-sections of resin-embedded granules were prepared using the microtome and analyzed by TEM using an FEI Morgani 268 microscope (100 kV).

Composition, Structure, and Acidity: The Si and Al content in the solids was determined by atomic absorption spectroscopy (AAS) using a Varian SpectraAA 220 FS spectrometer.

Powder XRD was conducted with a PANalytical X'Pert-Pro diffractometer (Bragg-Brentano geometry) using Ni-filtered Cu K α radiation ($\lambda = 0.1541$ nm). XRD patterns were taken in the range of 5–60° 2 θ , with an angular step size of 0.05° and a counting time of 8 s per step. Powdered and granulated samples were ground, and a fixed sample volume was irradiated, supported on a flat specimen holder.

Dry laser diffraction measurements of the zeolite powders were undertaken to characterize the particle size distributions using a Malvern Mastersizer MS2000 instrument.

Solid-state MAS NMR spectra of ^{27}Al and ^{29}Si were recorded at a spinning speed of 12.5 kHz on a Bruker Avance 400 MHz spectrometer featuring a 4 mm probe head and 4 mm ZrO_2 rotors. ^{29}Si spectra were acquired using 600 accumulations, 90° pulses with a length of 12.5 μs , and a recycle delay of 10 s. ^{27}Al spectra were collected using 2048 accumulations, 90° pulses with a length of 4.5 μs , and a recycle delay of 0.25 s. $(\text{NH}_4)\text{Al}(\text{SO}_4)_2 \cdot 12\text{H}_2\text{O}$ and octakis(trimethylsiloxy)silsesquioxane were used as reference materials for silicon and aluminum, respectively.

Thermal gravimetric analysis (TGA) was carried out in a Mettler Toledo TGA/SDTA851e microbalance. Measurements were performed ramping from 398 to 1173 K at 2 K min^{-1} in flowing dry air (35 $\text{cm}^3 \text{min}^{-1}$). Samples were pre-treated for 3 h at 398 K under a N_2 flow of 35 $\text{cm}^3 \text{min}^{-1}$ prior to analysis.

Infrared spectroscopy was performed under a N_2 flow (100 $\text{cm}^3 \text{min}^{-1}$) at 473 K using a Thermo Nicolet 5700 spectrometer equipped with a SpectraTech Collector II diffuse reflectance accessory and a high-temperature cell. Samples were dried at 673 K for 60 min, before the spectra were acquired in the range of 650–4000 cm^{-1} (nominal resolution of 4 cm^{-1} , 200 scans).

NH_3 -TPD was carried out in a Thermo TPDRO 1100 unit equipped with a thermal conductivity detector. The samples (100 mg) were pretreated at 823 K in a flowing He (20 $\text{cm}^3 \text{min}^{-1}$) for 2 h. NH_3 was adsorbed in three consecutive saturation cycles (10 vol% NH_3 in 20 $\text{cm}^3 \text{min}^{-1}$ He flow) at 473 K for 30 min followed by purging in He at the same temperature for 1 h. Desorption of NH_3 was monitored in the range of 473–873 K, ramping at 10 K min^{-1} .

Molecular Adsorption: Adsorption isotherms of cyclohexane (>99.5%, Sigma Aldrich), toluene (Fluka), and isopropyl alcohol (>99.5%, Sigma Aldrich) were measured at 298 K using an Intelligent Gravimetric Analyzer (IGA-002, Hiden Isochema). Adsorbent powders or granules (20 mg) were outgassed for 5 h at 573 K prior to analysis.

Supporting Information

Supporting Information is available from the Wiley Online Library or from the author.

Acknowledgements

Financial Support by the Swiss National Science Foundation (Project Number 200021-134572) is acknowledged. We thank the Electron Microscopy Center ETH Zürich (EMEZ) and the Swiss Light Source (SLS) at the Paul Scherrer Institute (Project Number 20110115).

Received: December 22, 2011

Published online: March 21, 2012

- [1] a) C. Sanchez, H. Arribart, M. M. Giraud Guille, *Nat. Mater.* **2005**, 4, 277; b) A. Stein, F. Li, N. R. Denny, *Chem. Mater.* **2008**, 20, 649; c) Z. Nie, A. Petukhova, E. Kumacheva, *Nat. Nanotechnol.* **2010**, 5, 15.
- [2] A. Corma, *Chem. Rev.* **1995**, 95, 559.
- [3] J. Pérez-Ramírez, C. H. Christensen, K. Egeblad, C. H. Christensen, J. C. Groen, *Chem. Soc. Rev.* **2008**, 37, 2530.
- [4] a) S. van Donk, A. H. Janssen, J. H. Bitter, K. P. de Jong, *Catal. Rev.* **2003**, 45, 297; b) F. Schüth, *Angew. Chem. Int. Ed.* **2003**, 42, 3604; c) M. Hartmann, *Angew. Chem. Int. Ed.* **2004**, 43, 5880; d) W.-C. Li, A.-H. Lu, R. Palkovits, W. Schmidt, B. Spliethoff, F. Schüth, *J. Am. Chem. Soc.* **2005**, 127, 12595; e) Q. Tan, X. Bao, T. Song, Y. Fan, G. Shi, B. Shen, C. Liu, X. Gao, *J. Catal.* **2007**, 251, 69; f) K. Egeblad, C. H. Christensen, M. Kustova, C. H. Christensen, *Chem. Mater.* **2008**, 20, 946; g) W. Schmidt, *ChemCatChem* **2009**, 1, 53; h) M. Choi, K. Na, J. Kim, Y. Sakamoto, O. Terasaki, R. Ryoo, *Nature* **2009**, 461, 246; i) K. P. de Jong, J. Zečević, H. Friedrich, P. E. de Jongh, M. Bulut, S. van Donk, R. Kenmogne, A. Finiels, V. Hulea, F. Fajula, *Angew. Chem. Int. Ed.* **2010**, 49, 10074; j) L. Lakiss, M. Rivallan, J.-M. Goupil, J. El Fallah, S. Mintova, *Catal. Today* **2011**, 168, 112; k) S. Lopez-Orozco, A. Inayat, A. Schwab, T. Selvam, W. Schwieger, *Adv. Mater.* **2011**, 23, 2602; l) J. Jiang, J. L. Jorda, J. Yu, L. A. Baumes, E. Mugnaioli, M. J. Diaz-Cabanas, U. Kolb, A. Corma, *Science* **2011**, 333, 1131; m) K. Möller, T. Bein, *Science* **2011**, 333, 297; n) V. Valtchev, E. Balanzat, V. Mavrodinova, I. Diaz, J. El Fallah, J.-M. Goupil, *J. Am. Chem. Soc.* **2011**, 133, 18950; o) K. Na, C. Jo, J. Kim, K. Cho, J. Jung, Y. Seo, R. J. Messinger, B. F. Chmelka, R. Ryoo, *Science* **2011**, 333, 328.
- [5] a) J. C. Groen, J. A. Moulijn, J. Pérez-Ramírez, *J. Mater. Chem.* **2006**, 16, 2121; b) J. C. Groen, J. A. Moulijn, J. Pérez-Ramírez, *Ind. Eng. Chem. Res.* **2007**, 46, 4193; c) D. Verboekend, J. Pérez-Ramírez, *Catal. Sci. Technol.* **2011**, 3, 879.
- [6] J. Pérez-Ramírez, S. Mitchell, D. Verboekend, M. Milina, N.-L. Michels, F. Krumeich, N. Marti, M. Erdmann, *ChemCatChem* **2011**, 3, 1731.
- [7] a) D. W. Breck, *Zeolite Molecular Sieves: Structure, Chemistry and Use*, Wiley-Interscience, New York **1974**; b) D. M. Ruthven, *Principles of Adsorption and Adsorption Processes*, John Wiley & Sons Inc., New York **1984**; c) S. Kulprathipanja, *Zeolites in Industrial Separation and Catalysis*, Wiley-VCH, Weinheim, Germany **2010**.
- [8] a) B. Stiles, T. A. Koch, *Catalyst Manufacture*, Marcel Dekker Inc., New York **1995**; b) F. Schüth, M. Hesse, in *Handbook of Heterogeneous Catalysis*, Vol. 1 (Eds: G. Ertl, H. Knözinger, J. Weitkamp), Wiley-VCH, Weinheim, Germany **2008**, Ch. 2.
- [9] a) D. S. Shihabi, W. E. Garwood, P. Chu, J. N. Miale, R. M. Lago, C. T.-W. Chu, C. D. Chang, *J. Catal.* **1985**, 93, 471; b) C. D. Chang, S. D. Helling, J. N. Miale, K. D. Schmitt, *J. Chem. Soc. Faraday Trans.* **1985**, 81, 2215; c) P. Canizares, F. Dorado, P. Sanchez, R. Romero, *Stud. Surf. Sci. Catal.* **2002**, 142, 707.
- [10] J. Rouquerol, G. V. Baron, R. Denoyel, H. Giesche, J. Groen, P. Klobes, P. Levitz, A. V. Neimark, S. Rigby, R. Skudas, K. Sing, M. Thommes, K. Unger, *Microporous Mesoporous Mater.* **2012**, 154, 2.
- [11] A. V. Neimark, P. I. Ravikovitch, *Microporous Mesoporous Mater.* **2001**, 44–45, 697.
- [12] P. L. Llewellyn, J.-P. Coulomb, Y. Grillet, J. Patarin, H. Lauter, H. Reichert, J. Rouquerol, *Langmuir* **1993**, 9, 1846.
- [13] M. Stampanoni, A. Groso, A. Isenegger, G. Mikuljan, Q. Chen, A. Bertrand, S. Henein, R. Betemps, U. Frommherz, P. Böhler, D. Meister, M. Lange, R. Abela, *Proc. SPIE* **2006**, 63180, 63180M.
- [14] I. L. C. Buurmans, J. Ruiz-Martínez, W. V. Knowles, D. van derBeek, J. A. Bergwerff, E. T. C. Vogt, B. M. Weckhuysen, *Nat. Chem.* **2011**, 3, 862.
- [15] M. H. F. Kox, A. Mijovilovich, J. J. H. B. Sättler, E. Stavitski, B. M. Weckhuysen, *ChemCatChem* **2010**, 2, 564.
- [16] a) R. von Ballmoos, W. M. Meier, *Nature* **1981**, 289, 782; b) E. G. Derouane, S. Determerie, Z. Gabelica, N. Blom, *Appl. Catal.* **1981**, 1, 201.
- [17] a) R. M. Dessau, E. W. Valyocsk, N. H. Goeke, *Zeolites* **1992**, 12, 776; b) J. C. Groen, T. Bach, U. Ziese, A. M. Paulaime-van Donk, K. P. de Jong, J. A. Moulijn, J. Pérez-Ramírez, *J. Am. Chem. Soc.* **2005**, 127, 10792.
- [18] N. Danilina, F. Krumeich, S. A. Castelanelli, J. A. van Bokhoven, *J. Phys. Chem. C* **2010**, 114, 6640.
- [19] H. W. Habgood, *Can. J. Chem.* **1958**, 36, 1384.
- [20] K. Shams, S. J. Mirmohammadi, *Microporous Mesoporous Mater.* **2007**, 106, 268.
- [21] a) R. V. Jasra, B. Tyagi, Y. M. Badheka, V. N. Choudary, T. S. G. Bhat, *Ind. Eng. Chem. Res.* **2003**, 42, 3263; b) J. Sebastian, R. S. Pillai, S. A. Peter, R. V. Jasra, *Ind. Eng. Chem. Res.* **2007**, 46, 6293.
- [22] F. Marone, B. Münch, M. Stampanoni, *Proc. SPIE* **2010**, 7804, 10-1.
- [23] C. Hintermüller, F. Marone, A. Isenegger, M. Stampanoni, *J. Synchrotron Rad.* **2010**, 17, 550.